Corrosion Science 222 (2023) 111382

Contents lists available at ScienceDirect

Corrosion Science

journal homepage: www.elsevier.com/locate/corsci

Impact of residual cementite on inhibition of CO_2 corrosion of mild steel

Shuai Ren [a,*], Xi Wang [a], David Young [a], Maalek Mohamed-Said [b], Bernardo Santos [a,1], Yi He [a], Marc Singer [a]

[a] Institute for Corrosion and Multiphase Technology, Department of Chemical and Biomolecular Engineering, Ohio University, Athens, OH 45701, USA
[b] TotalEnergies, OneTech - CSTJF, F-64018 Pau, France

ARTICLE INFO

Keywords:
Residual cementite
Steel microstructure
CO_2 Corrosion
Corrosion inhibition
Galvanic corrosion
Potentiodynamic polarization

ABSTRACT

A thick cementite skeleton exposed on a ferritic-pearlitic C1018 steel surface after pre-corrosion significantly compromised inhibition efficiency. However, this detrimental effect was insignificant for a lower carbon X65 steel with dispersed cementite microstructure, due to the insignificant amount of cementite that remained on its surface after pre-corrosion. After normalizing the increased cathodic area in the presence of residual cementite back to original area, both anodic and cathodic reactions were inhibited to the same extent as on bare steel with a sufficient inhibitor concentration. However, the detrimental effect of cementite cannot be completely eliminated due to its galvanic coupling effect.

1. Introduction

Internal corrosion of transmission pipelines associated with oil and gas production has always been a challenging issue for corrosion engineers [1,2]. Amongst different mitigation strategies, corrosion inhibitors (CIs) are often considered the first choice in handling internal corrosion due to their high efficiency and cost-effectiveness. As the most popular CI category, organic corrosion inhibitors function by developing a thin film bonded on the steel surface to decrease rates of electrochemical reactions [3,4]. They usually can deliver excellent inhibition efficiency on freshly polished steel surfaces under laboratory study conditions. In aged pipelines, however, the internal wall is often covered with various corrosion residues and/or corrosion products, such as residual cementite (Fe_3C) and precipitated siderite ($FeCO_3$) as well as different forms of iron sulfides (Fe_xS_y) [5–7]. The presence of corrosion residues or corrosion products can significantly affect the inhibition performance of organic corrosion inhibitors [8–11]. Therefore, understanding their effects on corrosion inhibition is of great benefit in applying corrosion inhibitors to tackle internal corrosion issues, particularly in aged pipelines.

Carbon steels are the most economical pipeline materials and widely used for hydrocarbon production and transmission. More or less, these steels contain a certain amount of cementite in their microstructures depending on their carbon contents. In other words, cementite, *i.e.*, iron carbide (Fe_3C), constitutes an original portion of any carbon steel. During the corrosion of carbon steel, ferrite dissolves and cementite remains on the surface. The residual Fe_3C can act as an additional cathodic reaction site because it is an electrical conductor with a lower overpotential [12,13]. As a result, it can accelerate the rate of iron dissolution *via* galvanic corrosion with ferrite.

The effect of residual Fe_3C on corrosion inhibition has been studied, but typically is limited to comparing the inhibition efficiency (IE) with and without or less Fe_3C residue, including before and after pre-corrosion, with different pre-corrosion durations, before and after removal of the residual Fe_3C, considering different steel composition and microstructure and using pure iron as a control group [8,9,14–21]. The primary conclusion is that residual Fe_3C has a detrimental effect on inhibitor performance as a source of additional cathodic sites, which is related to the microstructure and carbon content of mild steels [8,15,17,22]. In general, quenched and tempered steels with bainite or martensite-derived structures usually suffer less such effect compared with steels with ferritic-pearlitic structure. The Fe_3C in bainitic or martensitic steels could rapidly detach from the steel surface during corrosion, while the Fe_3C in pearlite tends to stay on the steel surface. In comparison with low-carbon steel, high-carbon steel generally showed a more pronounced effect due to more exposed Fe_3C residues. Xiong, et al. [14] demonstrated that the decreased inhibition efficiency after pre-corrosion was not related to the increased substrate roughness, *i.e.*, anodic area. Most of these studies [8,14–16] found that higher inhibitor dosage can help to combat the impact of the residual Fe_3C.

However, none of the above studies evaluated the detrimental effect

* Corresponding author.
E-mail address: sr100418@ohio.edu (S. Ren).
[1] Present address: Rua Antonio Martins Ferreira, 31, Sao Joao del Rei, MG, 36307724, Brazil

https://doi.org/10.1016/j.corsci.2023.111382
Received 3 April 2023; Received in revised form 28 June 2023; Accepted 4 July 2023
Available online 5 July 2023

due to the presence of iron carbide quantitatively, associating the increased cathodic area from residual Fe_3C or accelerated corrosion rate due to a galvanic coupling effect with the corresponding decreased inhibition efficiency, since it is difficult to develop a well-defined Fe_3C structure and measure its surface area. Some studies [8,9] postulated the interaction between inhibitor molecules and residual Fe_3C, such as by impeding the mass transfer of inhibitor molecules to the steel substrate, however, no direct evidence was provided. Besides, some studies [17,20] did not control the ferrous ion or hydrogen ion concentration in their experiments, which led to the increase of pH and $FeCO_3$ precipitation. Almost no study monitored or reported the residual concentration of corrosion inhibitor during their experiments. All these uncontrolled or unmeasured factors limited the result interpretation in these studies. In summary, the effect of residual Fe_3C on corrosion inhibition has not been quantitatively evaluated and the associated inhibition mechanism is not fully understood. Quantitative work with well-controlled water chemistry is required to have a better understanding of this effect.

The objective of this study is to quantitatively evaluate the effect of residual Fe_3C on the kinetics of anodic and cathodic reactions and, by virtue of this, assessing its detrimental effect on corrosion inhibition. In this work, a pure and definable Fe_3C skeleton was developed after 2-days of pre-corrosion and characterized by X-ray diffraction (XRD), scanning electron microscopy (SEM), and energy dispersive X-ray spectroscopy (EDS). Electrochemical assessments, including linear polarization resistance (LPR) and potentiodynamic polarizations, were utilized to monitor corrosion evolution and inhibitor performance during long-term exposure. Specimen weight loss was also monitored. Finally, the effect of residual cementite on corrosion inhibition was quantitatively evaluated and compared between C1018 and X65 steels with different microstructures and carbon contents. In this work, ferrous ion and hydrogen ion concentrations were well-controlled and corrosion inhibitor concentration was monitored throughout the experiments.

2. Experimental

2.1. Materials

Steel specimens were machined from a UNS G10180 carbon steel (C1018) with a ferritic-pearlitic microstructure and an API 5 L X65 carbon steel (X65) with ferrite grains with small and dispersed cementite precipitates, as shown in Fig. 1. The composition of the studied C1018 and X65 steels are provided in Table 1. The carbon content of C1018 is three times that of X65. By lever rule in the Fe-C phase diagram, the Fe_3C content in the C1018 (2.28 wt%) is three times that of the X65 (0.69 wt %). In addition, the C1018 microstructure displays large pearlite (alternating lamellae of α-ferrite and cementite) grains, while the X65 does not. Due to these different steel microstructures and carbon contents, the effect of residual Fe_3C on corrosion inhibition is expected to be different between the C1018 and X65 steels.

2.2. Equipment and conditions

The experiments were carried out using a 4 L glass cell with an impeller and connected to a ferrous ion concentration controller *via* a flow loop, as shown in Fig. 2. A detailed introduction about this setup has been reported elsewhere [23,24]. This experimental configuration allows for exposure of 7 specimens to the corrosive environment, including working electrodes (WE) and immersion specimens for weight loss (WL) measurement and surface characterization. Immersion specimens were masked with Xylan coating, and the working electrodes were mounted in high temperature epoxy. In addition, the setup gives superior control of species diffusion in solution by an impeller to simulate the flow condition in a pipeline. All specimens, at the same radial distance from the impeller, experienced identical flow conditions, *i.e.*, the same mass transfer coefficient and shear stress. The mass transfer correlation for the impeller-created flow in this setup was determined by equating the mass transfer coefficient from limiting currents of the ferri-ferrocyanide redox reaction [25], as shown in the following equation.

$$Sh = 2.94\mathrm{Re}^{0.55}Sc^{0.33} \quad (1)$$

The rotational speed of the impeller was set at 52 rpm throughout these experiments, which would create a flow equivalent to a 1.6 m/s single phase water flow in a pipe with an inner diameter of 0.1 m and a shear stress of 4.7 Pa.[2]

The full test matrix is listed in Table 2. All the experiments were conducted at 55 °C in deoxygenated 5 wt% NaCl solution, a simulated exploration and production environment where the produced water often contains a high salt concentration [26]. The pH was maintained at 4.5 ± 0.1 by injecting deoxygenated $NaHCO_3$ or HCl solutions as appropriate. Sparging with CO_2 was maintained throughout the experiment to prevent air ingress and saturate the test electrolyte with CO_2. Prior to each experiment, all the specimens were polished with up to 600 grit abrasive papers in isopropanol flow, cleaned with isopropanol in an ultrasonic bath, air-dried, and weighted before insertion into the cell. An imidazoline-type commercial inhibitor package was employed in this work. The ferrous ion concentration was controlled at a low level during 2-days of pre-corrosion by ion-exchange media to avoid any formation of $FeCO_3$.

2.3. Experimental procedure and techniques

The experimental procedure includes two stages: pre-corrosion stage and inhibition stage, as indicated in Fig. 3. After two hours of saturating the electrolyte with CO_2, two carbon steel working electrodes (WE #1 and #2) and four immersion specimens for weight loss measurement or surface analysis were inserted into the solution. The corrosion rate (CR) and corrosion potential (or open circuit potential, OCP) were recorded by linear polarization resistance (LPR) measurement periodically. These specimens were pre-corroded for two days and one of the specimens was then retrieved for surface characterization. At the beginning of day 3, a third working electrode (WE #3), freshly polished and without pre-corrosion, was introduced into the glass cell, and an initial corrosion rate was recorded. Then, the first dose of 100 ppm_w corrosion inhibitor was injected into the solution. When the corrosion rate stabilized, the potentiodynamic polarizations were conducted on WE #1. The second dose of 100 ppm_w inhibitor was then injected into the glass cell and the same steps of corrosion rate monitoring and polarizations were repeated as conducted after the first inhibitor injection. When the corrosion rate did not significantly decrease further with additional doses of inhibitor, the inhibition stage ended and potentiodynamic polarizations were conducted on all three working electrodes. Multiple polarization curves were collected with WE #1, which could result in the risk of altering inhibited surface condition after each time of polarization. Therefore, WE #2 with the same pre-corrosion condition was exposed but only polarized at the end of the experiment duration to validate the polarization curves collected on WE #1. Throughout the experiment, immersion specimens were retrieved periodically for weight loss measurements and surface characterization, and the concentration of Fe^{2+} and inhibitor was measured every 24 h. The experiment was conducted twice following the above procedure, and one series of characteristic LPR and polarization curves is shown in this paper.

A three electrode configuration was used for electrochemical experiments, with carbon steel specimens as working electrodes, a platinum grid as a counter electrode and a Ag/AgCl reference electrode with saturated KCl. To monitor three different working electrodes simultaneously, a Multiplexer (ECM8, Gamry) was connected to a potentiostat

[2] Estimated using software FREECORP, ICMT, Ohio University.

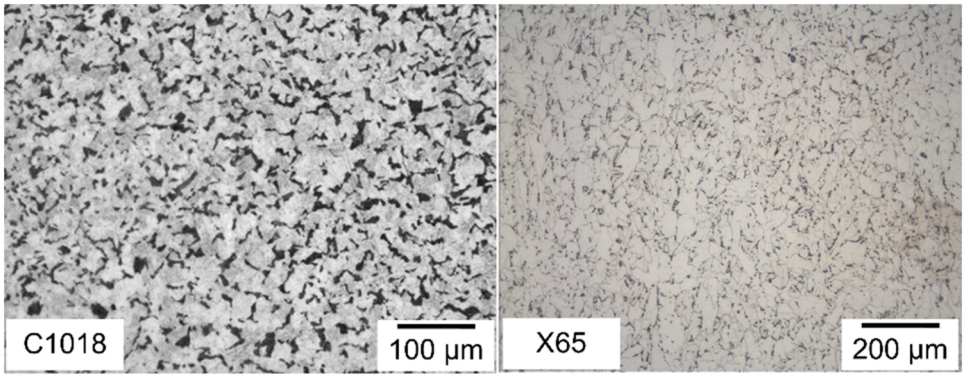

Fig. 1. Optical images of the C1018 (left) and X65 (right) microstructures, after Nital etch, used in this work.

Table 1
Composition (wt%) of C1018 and X65 steels used in the present work.

%	C	Mn	Si	Ni	Cu	Cr	Mo	S	Al	V	Ti	Nb	P	Fe
C1018	0.16	0.65	0.25	0.06	0.09	-	0.02	0.010	0.007	0.002	0.001	0.002	0.009	bal.
X65	0.05	1.40	0.22	0.24	0.11	0.23	0.07	< 0.001	0.023	0.035	0.011	0.036	0.003	bal.

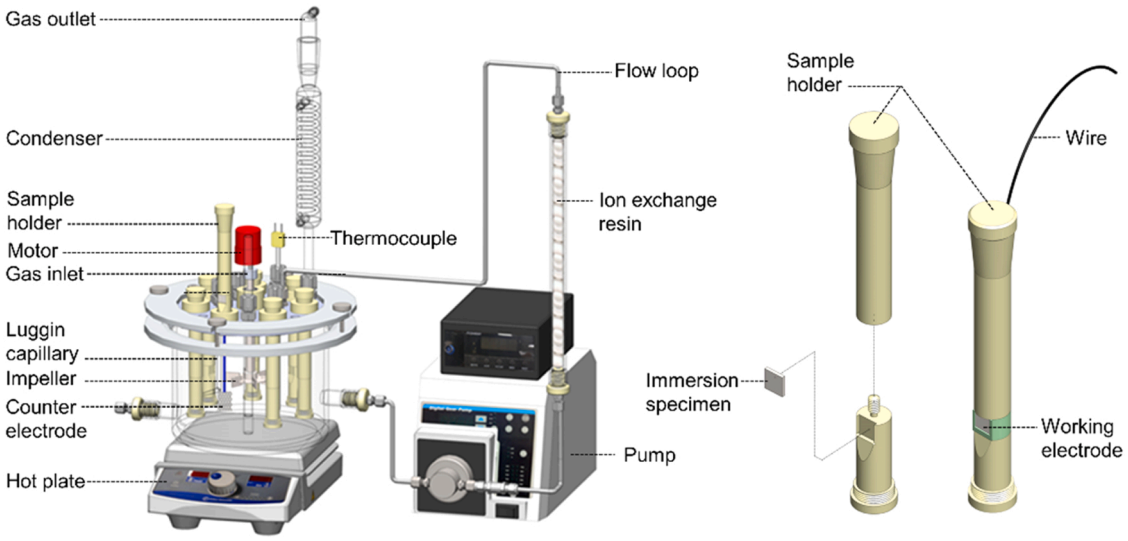

Fig. 2. The schematic of experimental equipment: 4 L glass cell with impeller connected ferrous ion controller (left) and sample holders with immersion specimen and working electrode (right)[31].

Table 2
Experimental conditions of this work.

Parameter	Description
Electrolyte	5 wt% NaCl (3-liter)
Materials	C1018 and X65 carbon steels
Working electrodes	Flat square, 1.6 cm^2
Immersion specimens	Flat square, 1.6 cm^2
Temperature	55 ± 2 °C
Total pressure	1 bar
CO_2 partial pressure	0.86 bar (saturated)
pH	4.5 ± 0.1
Corrosion inhibitor	0 – 400 ppm_w (Imidazoline-type commercial package)
Fe^{2+} concentration	Controlled and monitored
Flow condition	Same mass transfer coefficient as a flow of 1.6 m/s in a pipe with an inner diameter of 0.1 m (shear stress: 4.7 Pa)

(Interface 1010, Gamry), and the measurements of each working electrode were collected alternately against the same counter and reference electrode. LPR scan range was from −5 mV to + 5 mV *vs.* OCP with a scan rate of 0.125 mV/s, and a B value of 26 mV [27] was used for corrosion rate calculation *via* the Stern-Geary equation [28]. Cathodic potentiodynamic polarization sweeps were conducted by starting from the OCP at a scan rate of 0.125 mV/s. The anodic potentiodynamic sweeps were taken with the same scan rate subsequently when the OCP returned to the original value before the cathodic sweep. The ohmic drop was compensated in all curves. Retrieved immersion specimens were rinsed by deionized water and isopropyl alcohol, and then air-dried before the specimens weighing and then top-view scanning electron microscopy (SEM) and energy dispersive X-ray spectroscopy (EDS) analysis were conducted. Since precipitated corrosion products (*e.g.*, $FeCO_3$) should not be expected due to well-controlled water chemistry, and since residual cementite should be retained for further characterization, no conventional corrosion product cleaning procedure was implemented for weight loss measurement in this work. Due to the

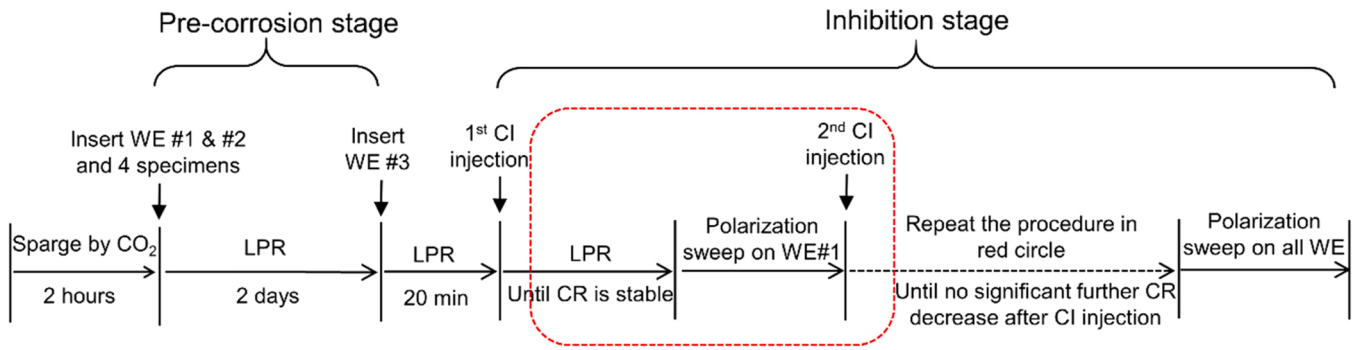

Fig. 3. Schematic of the experimental procedure.

residual cementite is the undissolved portion of steels, the weight loss used for corrosion rate evaluation should not include the weight of residual cementite and only dissolved ferrite was counted. Specimen thickness loss was calculated from weight loss with knowing iron density of 7.87 g/cm^3 and specimen surface area (Table 2). It is noteworthy that the weight of residual cementite was not accounted into the weight loss used for the calculation of thickness loss, which was insignificant due to its low mass percentage of cementite in C1018 (2.28 wt%) and X65 (0.69 wt%). To characterize the cross-sections of these specimens, they were mounted in epoxy, finished with a fine polish using 0.25 μm diamond suspension, and sputter coated with a thin layer of palladium. The secondary electron images and EDS data (JSM-6390LV, JEOL) were taken with an accelerating voltage of 15 kV, a working distance of 14–15 mm, and a spot size of 50–60. X-ray diffraction (XRD) was conducted using an X-ray diffractometer (Miniflex 600, Rigaku) with monochromatic CuKα radiation ($\lambda = 0.15405$ nm) at a scan rate of 3°/min with a 0.02° step width. The concentration of Fe^{2+} was measured by a spectrophotometer (Genesys 10vis, Thermo Scientific) and a commercial phenanthroline-containing reagent (FerroVer Iron Reagent, Hach) was used in this procedure. The concentration of corrosion inhibitor was measured by a UV-Vis spectrophotometer (Cary 60, Agilent) following the methyl orange method [29,30], a widely used technique for the analysis of cationic organic species in corrosion inhibitors.

3. Results and discussion

3.1. Corrosion rate and inhibition efficiency

The corrosion rate and potential evolution of three C1018 working electrodes during pre-corrosion and inhibition stages are displayed in Fig. 4. During the 2-day pre-corrosion step, the corrosion rates of WE #1 and #2 kept increasing; this stems from their acceleration due to exposed Fe_3C serving as an additional cathodic reaction area. After 2-days of pre-corrosion, an essentially pure Fe_3C layer was expected to be formed on the specimen surface. After injecting the 1st dose of the corrosion inhibitor (100 ppm_w), the corrosion rates of WE #1 and #2 decreased and then stabilized at *ca.* 0.8 mm/year. The 2nd corrosion inhibitor injection inhibited the corrosion rates further to *ca.* 0.27 mm/year. However, the corrosion rates of WE #1 and #2 did not decrease significantly after additional 3rd and 4th inhibitor doses, stabilizing at *ca.* 0.18 mm/year.

On day 3, a freshly polished working electrode, WE #3, was added to the glass cell. The corrosion rate of WE #3 without pre-corrosion decreased sharply to *ca.* 0.1 mm/year after the addition of the 1st dose of inhibitor and stabilized at *ca.* 0.08 mm/year after three additional doses. Unambiguously, corrosion of the pre-corroded specimens possessing iron carbide residues was not as effectively inhibited as the bare specimen after injection of the first dose of corrosion inhibitor. At the end of the experiment, the minimum inhibited corrosion rate (0.18 mm/year) with pre-corrosion was still higher than that (0.08 mm/year) without pre-corrosion. These inhibition differences between pre-corroded and bare specimens must be related to the residual Fe_3C exposed during pre-corrosion.

Corrosion potential evolution was then analyzed using acquired potentiodynamic polarization results, as discussed below. It is noteworthy that corrosion rate jumps and corresponding potential drops of WE #1 right before the 2nd and 3rd corrosion inhibitor injections were because of the conducting of polarization sweeps disrupting the specimen surface. However, their values rapidly recovered back to similar levels of WE #2 (no polarization sweep was conducted until the very end of the experiment) after each dose of inhibitor injection. This commercial inhibitor showed rapid adsorption kinetics and will be further discussed in the below section on polarization curves.

The corrosion rate and potential evolution of three X65 working electrodes during pre-corrosion and inhibition stages are displayed in Fig. 5. During the 2-day pre-corrosion step, the corrosion rates of WE #1 and #2 increased to 6–7 mm/year in the first 12 h and then remained at this rate for 2 days. This stabilized corrosion rate after 2-day pre-corrosion is lower than that (11–12 mm/year) on C1018, which was related to the lesser presence of more easily detachable Fe_3C particles on the X65 specimen. After injecting the 1st dose of inhibitor (100 ppm_w), the corrosion rates of WE #1 and #2 decreased and then stabilized at *ca.* 0.24 mm/year, which was also lower than that (0.8 mm/year) on C1018. The 2nd corrosion inhibitor injection further decreased the corrosion rates to around 0.1 mm/year. However, no significant corrosion rate decrease was observed after the 3rd and 4th doses, stabilizing at *ca.* 0.07 mm/year; it was significantly lower than that observed on C1018 (0.18 mm/year), again implying much less Fe_3C on the X65 specimen after pre-corrosion. The corrosion rate of WE #3 without pre-corrosion decreased sharply to *ca.* 0.06 mm/year after the 1st corrosion inhibitor dosage and stabilized at *ca.* 0.03 mm/year without a significant decrease after three additional doses. The potential evolutions displayed a similar increasing trend as observed with C1018 steel and will be further discussed in the below polarization curves section.

The inhibition efficiencies (IE) of C1018 and X65 steels with different surface conditions and various inhibitor concentrations were calculated *via* the following equation with their results presented in Fig. 6.

$$IE = (1 - CR_{inh}/CR_{un}) \times 100\% \quad (2)$$

"CR_{un}" refers to the uninhibited corrosion rates before pre-corrosion. "CR_{inh}" refers to the inhibited corrosion rates with different concentrations of corrosion inhibitor. Under bare surface condition (no pre-corrosion), 100 ppm_w inhibitor achieved near 100% inhibition efficiency on both C1018 and X65 steels. After a 2-day pre-corrosion step, the inhibition efficiency for C1018 with 100 ppm_w inhibitor showed a substantial drop from 98% to 83%. In comparison, the inhibition

[3] Images courtesy of Cody Shafer, ICMT, Ohio University.

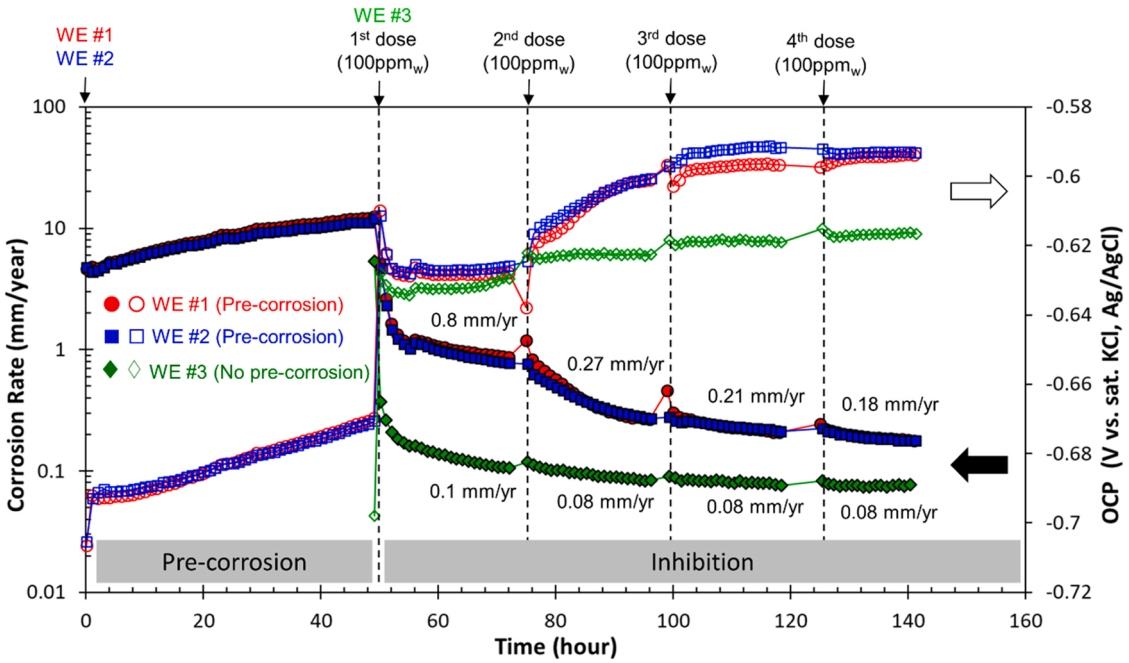

Fig. 4. Corrosion rate and potential evolution of three C1018 working electrodes during pre-corrosion and inhibition stages. WE #1 and #2 are 2-day pre-corroded electrodes. WE #3 is a freshly polished electrode. Stabilized corrosion rates before each additional inhibitor dose are labelled in the figure. Each solid data series refer to corrosion rate, and hollow data series refer to OCP.

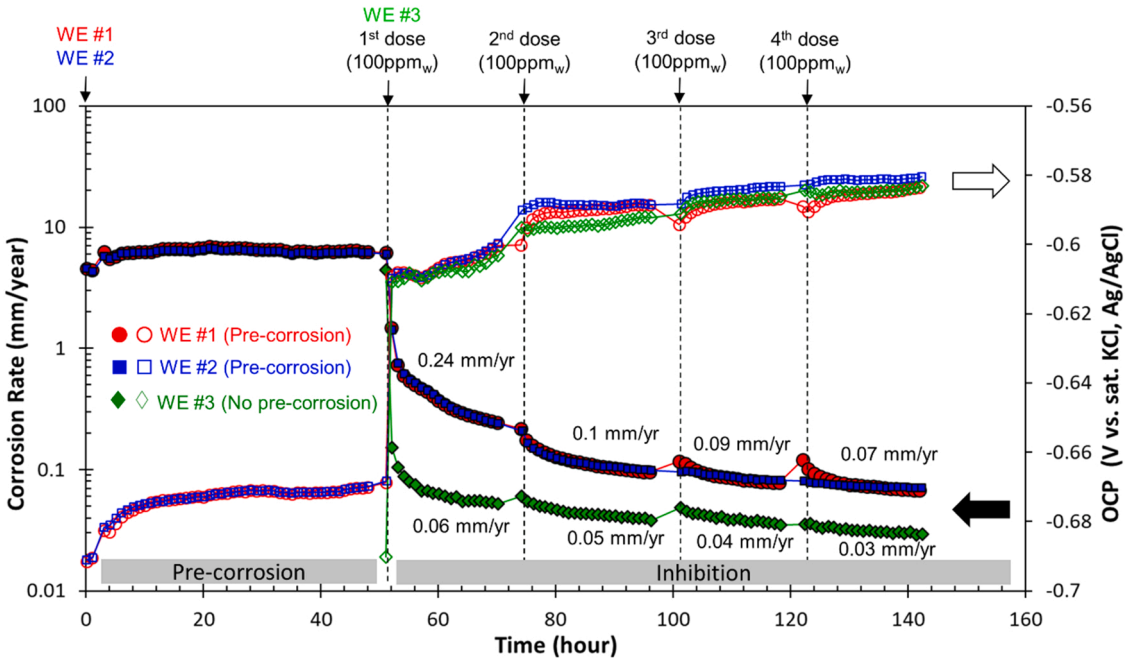

Fig. 5. Corrosion rate and potential evolution of three X65 working electrodes during pre-corrosion and inhibition stages. WE #1 and #2 are pre-corroded electrodes. WE #3 is a freshly polished electrode. Stabilized corrosion rates before each additional inhibitor dose are labelled in the figure. Each solid data series refer to corrosion rate, and hollow data series refer to OCP.

efficiency of X65 was still higher than 90% and the drop was very limited, consistent with different Fe_3C layer characteristics on C1018 and X65 specimens after pre-corrosion. With 200 ppm_w inhibitor, the inhibition efficiency of C1018 was increased to 94%. With 300 and 400 ppm_w inhibitor, both steels after pre-corrosion were well inhibited, suggesting higher dosage is beneficial to combating the adverse effect of residual Fe_3C [14,16,22].

The measured concentrations of commercial inhibitor and Fe^{2+} and calculated steel thickness loss values *via* weight loss measurements are listed in Table 3. After 96 h in the experiment with C1018, 200 ppm_w inhibitor (2 doses of 100 ppm_w each) was added in the glass cell, as indicated by target concentration. However, the measured concentration was 116 ± 3 ppm_w. The decrease of bulk inhibitor concentration could be related to its adsorption on residual Fe_3C (large area due to high porosity) and other interfaces, such as the water-air interface, the surface of sample holders and impeller, and the wall of the glass cell. After

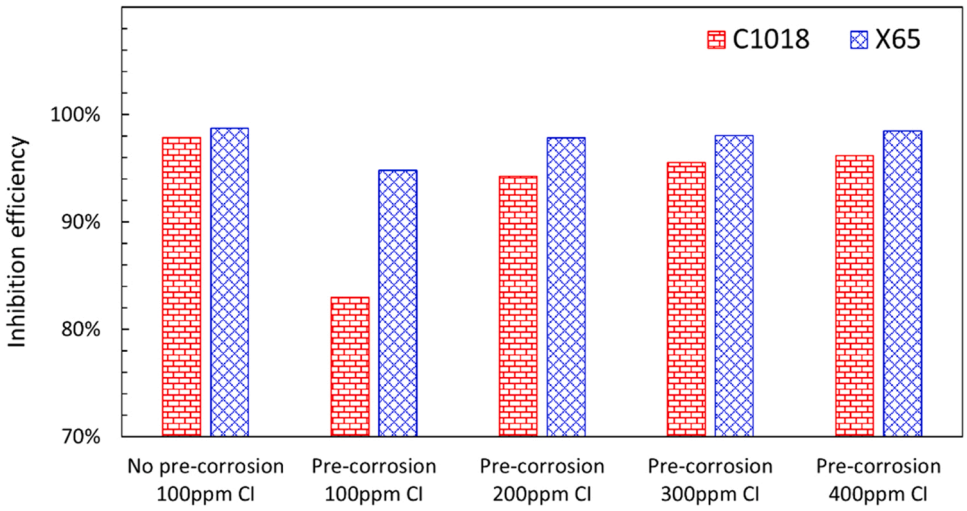

Fig. 6. Comparison of inhibition efficiencies of C1018 and X65 steels with different surface conditions and increasing inhibitor concentrations.

Table 3
Measured concentrations of corrosion inhibitor and ferrous ion and calculated steel thickness loss value *via* weight loss at different times.

Time (hour)		48	72	96	120	148
Target CI concentration (ppm_w)		0	100	200	300	400
C1018	Measured CI concentration (ppm_w)*	-	-	116 ± 3	205	310
	Fe^{2+} concentration (ppm_w)	2.5	-	7.2	9.2	-
	Calculated thickness loss *via* WL (μm)	41	42	44	42	-
X65	Measured CI concentration (ppm_w)*	-	71	136	228	279 ± 7
	Fe^{2+} concentration (ppm_w)	1.2	2.7	2.9	3.0	3.1
	Calculated thickness loss *via* WL (μm)	27	28	-	-	29

* 1st CI injection was at 48 h and all CI concentrations were measured 24 h later after their injections. The concentrations of inhibitor and Fe^{2+} at 72 hrs in the test of C1018 were not available due to lack of measurement.

injecting the 3rd and 4th corrosion inhibitor doses, the increased values of measured concentration were consistent with the increased values of target concentration suggesting an insignificant consumption. A similar trend was observed in the experiment involving the X65 steel specimens. Decreases in inhibitor concentration in a closed system were also reported by other researchers [31] and continuous inhibitor injection is suggested in future work for maintaining a constant concentration.

Fe^{2+} concentration was below 10 ppm_w throughout the experiments (Table 3) because it was well-controlled by ion-exchange media in the first 48 h, where iron dissolved at a high rate, then iron dissolution was diminished after the injection of corrosion inhibitor. This suggested that $FeCO_3$ should not precipitate on the steel surface in both experiments. The average corrosion rates according to weight loss were consistent with the integrated corrosion rates measured by LPR throughout the exposure time periods, validating the selection of B value in corrosion rate calculations using the Stern-Geary equation [28]. The estimated steel thickness loss after 2-day pre-corrosion was *ca.* 41 μm for C1018 and *ca.* 27 μm for X65 specimens. The difference of thickness loss was caused by the different corrosion rates during pre-corrosion, which was related to the different residual Fe_3C conditions. During the inhibition stage, the steel thickness loss did not significantly increase for both C1018 and X65 specimens, since the corrosion was effectively inhibited.

3.2. Specimen surface characterization

The XRD patterns of C1018 and X65 specimens after 2-day pre-corrosion are shown in Fig. 7. Residual Fe_3C was clearly detected on C1018 owing to its microstructure and high carbon content. However, essentially no Fe_3C was found on X65, which could be related to low Fe_3C content and its detachment from the surface as corrosion proceeded. Besides, $FeCO_3$ was not detected on both steels suggesting $FeCO_3$ precipitation did not happen due to the well-controlled ferrous ion and hydrogen ion concentrations throughout the experiments.

The top-view and cross-sectional SEM images of C1018 specimens retrieved at different times during the experiment are shown in Fig. 8. After 2-day pre-corrosion, a pronounced Fe_3C residue was exposed on the C1018 steel surface after the dissolution of ferrite. The thickness of this Fe_3C skeleton, derived from pearlite, was around 40 μm as determined from the cross-sectional SEM image as shown in Fig. 8(e). This measured thickness is consistent with the calculated steel thickness loss *via* weight loss (Table 3) indicating the intact Fe_3C structure remained on the steel surface after 2-day pre-corrosion. This explained why the corrosion rate kept increasing during the pre-corrosion stage. After injecting different doses of inhibitor, the appearance of a Fe_3C residue did not show any significant change, and its structure was still preserved completely after 4-days of inhibition. The thickness of the Fe_3C skeleton remained around 40 μm further indicating the effectiveness of the inhibition. It is noteworthy that no pitting or severe localized corrosion occurred throughout the test. Even though the residual cementite provided a massive cathode, the steel substrate still showed uniform corrosion thanks to the uniform distribution of the Fe_3C network (acting as cathodic sites) across the substrate during the pre-corrosion stage. After adding corrosion inhibitor, the substrate was uniformly inhibited without any preferential protection.

The top-view and cross-sectional SEM images of X65 specimens retrieved at different times during the experiment are shown in Fig. 9. After 2-day pre-corrosion, a mud crack-like morphology was observed on the X65 steel surface. Its composition was measured by EDS and will be discussed below. From cross-sectional view, an extremely thin and disconnected layer was observed on the X65 steel surface. Considering the calculated thickness loss of 27 μm *via* weight loss measurement (Table 3), most of the Fe_3C residue spalled from the surface during pre-corrosion. Only very limited amount of residual Fe_3C was available on the specimen surface to promote corrosion *via* galvanic coupling effect with ferrite. Therefore, the increase of corrosion rate was insignificant during pre-corrosion compared with that of C1018 steel. After injecting different doses of inhibitor, the top-view morphology did not show a

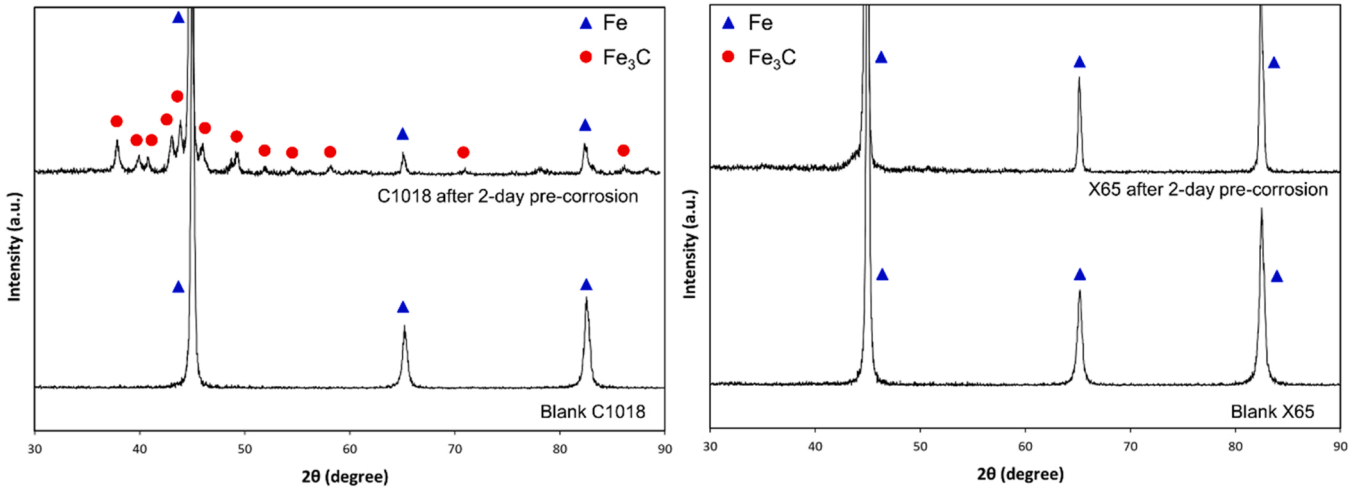

Fig. 7. XRD patterns of C1018 and X65 blank specimens and specimens after 2-day pre-corrosion.

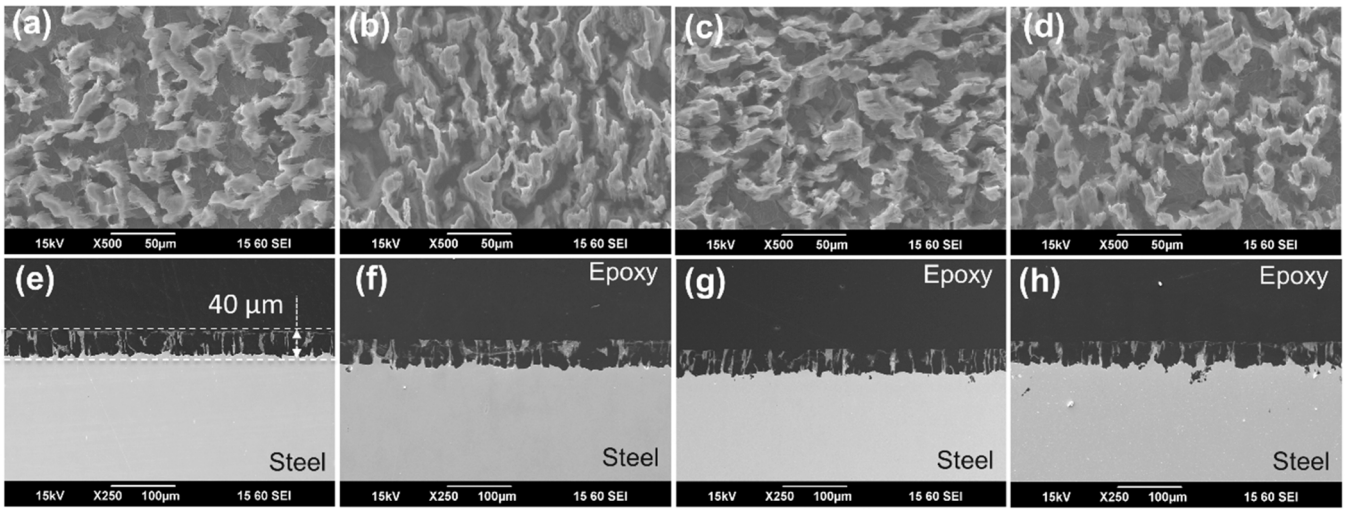

Fig. 8. The top-view and cross-sectional SEM images of C1018 specimens retrieved at different times during the experiment after: (a) and (e) 2-day pre-corrosion; (b) and (f) 2-day pre-corrosion and 1-day inhibition (100 ppm_w); (c) and (g) 2-day pre-corrosion and 2-day inhibition (200 ppm_w); (d) and (h) 2-day pre-corrosion and 4-day inhibition (400 ppm_w).

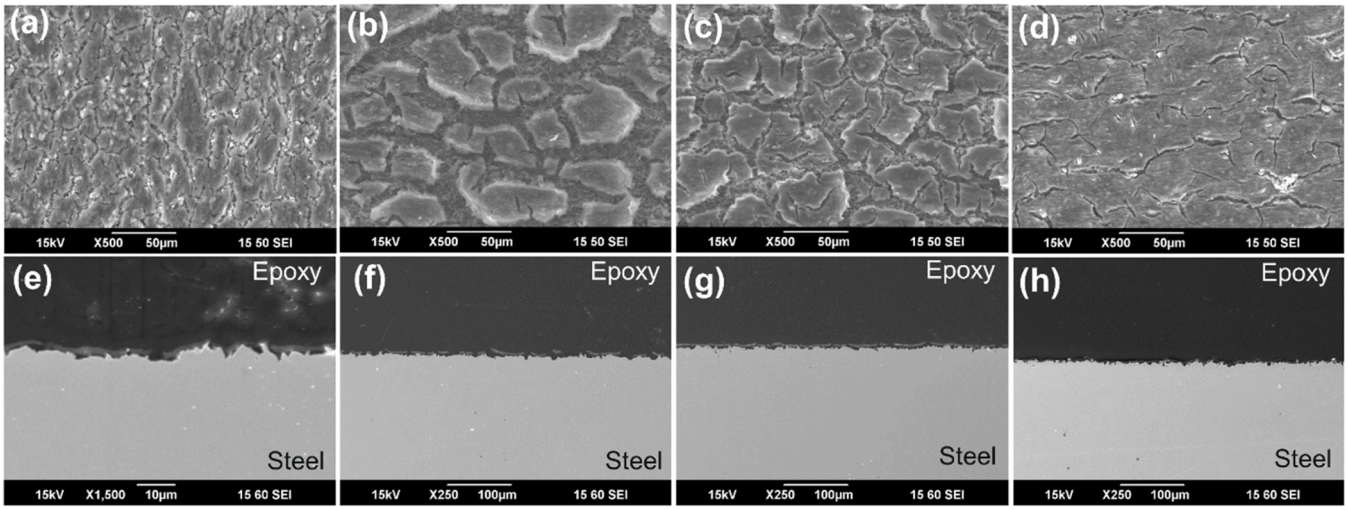

Fig. 9. The top-view and cross-sectional SEM images of X65 specimens retrieved at different times during the experiment after: (a) and (e) 1-day pre-corrosion; (b) and (f) 2-day pre-corrosion; (c) and (g) 2-day pre-corrosion and 1-day inhibition (100 ppm_w); (d) and (h) 2-day pre-corrosion and 4-day inhibition (400 ppm_w).

significant change. From the cross-sectional view, the steel surface was as bare as a freshly polished specimen. Hence, the inhibition efficiency loss of X65 steel after pre-corrosion was very limited without the influence of additional surface area as seen on the C1018 steel.

The EDS data measured from the top surface of the X65 specimen after 2-day pre-corrosion is shown in Fig. 10. Spectrum #1 was derived from the mud crack-like feature and spectrum #2 was acquired from the steel substrate. According to the measured atom percentage, a certain amount of carbon was detected in spectrum #1 suggesting the existence of Fe_3C residue on these mud crack-like features. However, this Fe_3C was thin and out of XRD measurable limit with our available instrumentation. Besides, a pronounced accumulation of alloying elements was found on these sites, such as Cr, Cu, and Al. In comparison, almost pure Fe was detected at the steel substrate. Overall, this mud crack-like structure and the accumulation of alloying elements on X65 specimen surfaces had very limited effect on the underlying corrosion process since the corrosion rate was stable throughout the pre-corrosion stage (Fig. 5).

3.3. Potentiodynamic polarization analysis

To understand the inhibition mechanism of anodic and cathodic reactions in the presence of residual Fe_3C, polarization curves obtained with different surface conditions and various inhibitor concentrations were compared and analyzed. The main anodic and cathodic reactions of CO_2 corrosion are shown in the following equations (the direct reductions of carbonic acid and bicarbonate (HCO_3^-) were considered to be insignificant [32,33]):

$$Fe(s) \rightarrow Fe^{2+}(aq) + 2e^- \quad (3)$$

$$2H^+(aq) + 2e^- \rightarrow H_2(g) \quad (4)$$

Flow also plays an important role in CO_2 corrosion *via* affecting the mass transfer rate of hydrogen ions and their donor species, such as carbonic acid, from the bulk solution to the steel surface. When the charge transfer rate of hydrogen ion reduction is faster than the mass transfer rate, corrosion rate will be controlled by the latter, which is reflected by the "limiting current region" in the cathodic potentiodynamic polarization curve. For most organic corrosion inhibitors, such as imidazolinium and quaternary ammonium salts, both anodic and cathodic reactions are usually retarded, without affecting limiting current since the inhibitor film adsorbed on the surface is not expected for a mass transfer barrier [34–37].

3.3.1. Polarization curves analysis and normalization of C1018 steel

The potentiodynamic polarization curves of C1018 steel under three different conditions, *i.e.*, no pre-corrosion and no inhibitor, no pre-corrosion and 400 ppm_w inhibitor, and 2-day pre-corrosion and no inhibitor, are shown in Fig. 11. After adding 400 ppm_w corrosion inhibitor (4 doses of 100 ppm_w each), both anodic and cathodic reactions on bare steel were retarded significantly, while the limiting current was unaffected compared to the condition without either pre-corrosion or corrosion inhibitor. As aforementioned, the corrosion rate was maximally inhibited by 400 ppm_w inhibitor, which indicates both anodic and cathodic reactions were retarded maximally. The corrosion changed from mass transfer control to charge transfer control after adding inhibitor, leading to a sharp corrosion potential increase (Fig. 4). After 2-day pre-corrosion, the limiting current of the hydrogen ion reduction reaction was significantly increased due to the exposed Fe_3C skeleton serving as an additional cathodic area. For the same reason, the charge transfer controlled part of the hydrogen ion reduction was expected to be accelerated to the same extent, which was not seen in the polarization curves since the corrosion was mass transfer controlled for the cathodic reaction. The minor retardation of the anodic reaction after pre-corrosion should be associated to the change of solution environment near the substrate surface in the Fe_3C skeleton, such as by increased ferrous ion concentration. Significant cathodic acceleration and slight anodic retardation led to an increasing trend of corrosion potential during the 2-day pre-corrosion (Fig. 4). It is noteworthy that the cathodic polarization curve after pre-corrosion doesn't show the real cathodic current density because cathodic area was increased by residual cementite compared with its original area (specimen surface area), which will be further discussed below.

The potentiodynamic polarization curves of C1018 steel with different concentrations of corrosion inhibitor after 2-day pre-corrosion are displayed in Fig. 12. After 2-day pre-corrosion and 1-day inhibition with 100 ppm_w inhibitor, both anodic and cathodic reactions were retarded, while the limiting current was unaffected compared with 2-day pre-corrosion condition without inhibitor. They were retarded further when the inhibitor concentration was increased to 200 ppm_w. However, there was no significant further retardation from 200 ppm_w to 400 ppm_w, suggesting maximum inhibition was achieved on the specimen that experienced 2-day pre-corrosion. In comparison with the case of no pre-corrosion but 400 ppm_w inhibitor, the inhibited anodic polarization curves overlapped, suggesting that the anodic reactions were retarded to the same extent regardless of surface condition.

However, the inhibited cathodic curves with pre-corrosion showed a pronounced difference from that without pre-corrosion. This difference was related to the additional cathodic reaction area owing to the exposed Fe_3C skeleton after pre-corrosion. As aforementioned, the inhibited cathodic polarization curves with and without pre-corrosion cannot be compared directly since the cathodic surface areas are different for each case. In the absence of pre-corrosion, the cathodic surface area is known (equal to the sample surface) and equal to the anodic surface area. In the presence of pre-corrosion, the cathodic surface area is increased due to the presence of Fe_3C and unknown, while the anodic surface area can be assumed to remain unchanged. To compare the cathodic inhibition with and without pre-corrosion from the cathodic polarization curves, the cathodic curve with pre-corrosion needs to be normalized based on the cathodic area on the bare surface.

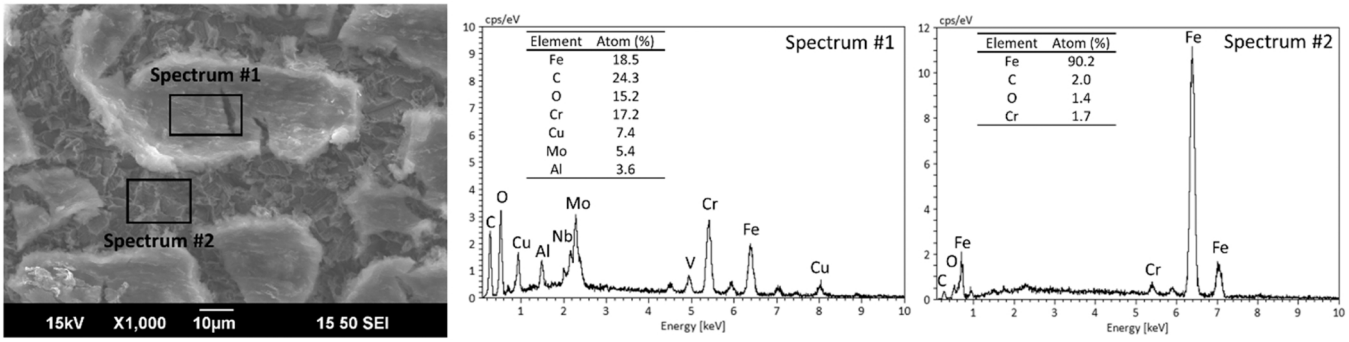

Fig. 10. The EDS results measured on the top surface of the X65 specimen after 2-day pre-corrosion (Fig. 9b).

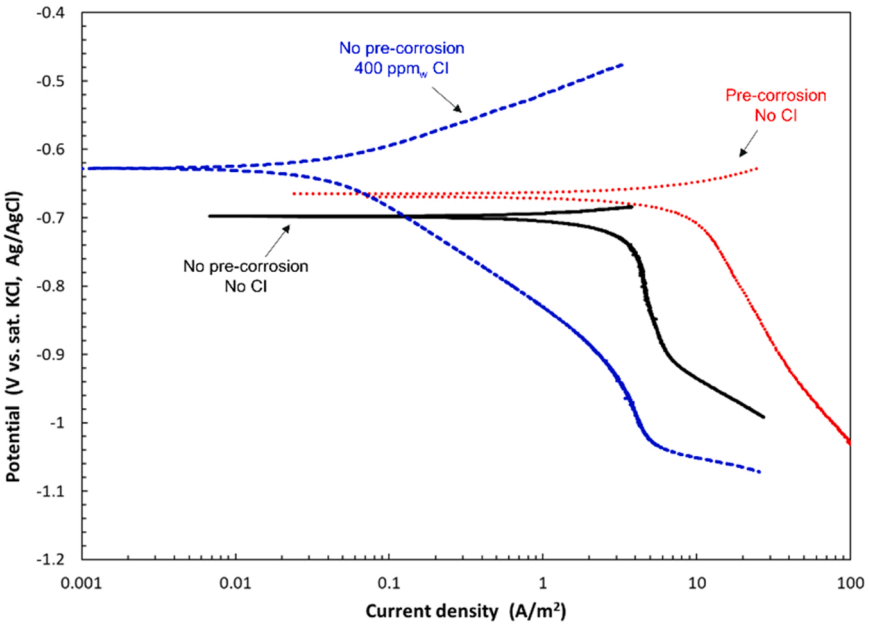

Fig. 11. The potentiodynamic polarization curves of C1018 steel under three different conditions.

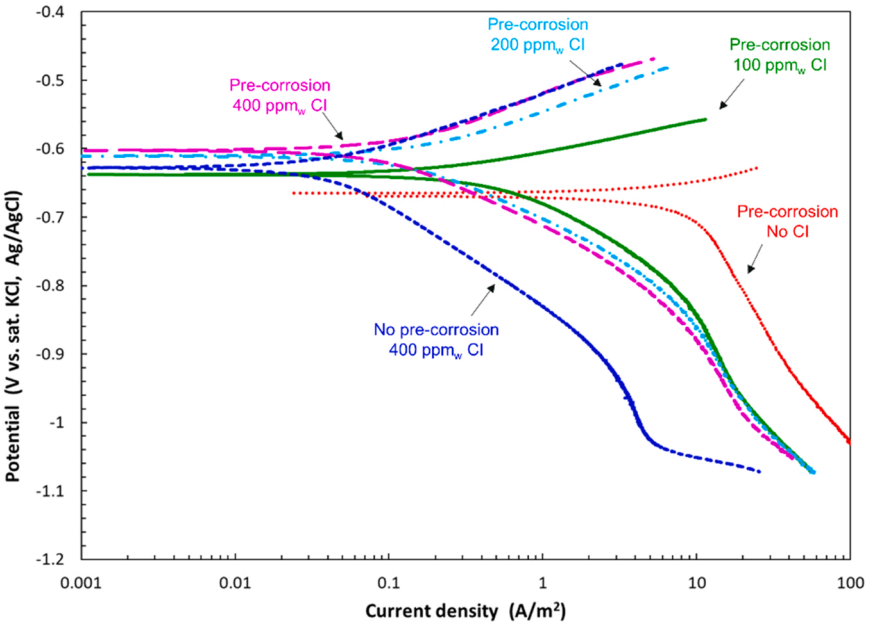

Fig. 12. The potentiodynamic polarization curves of C1018 steel with different corrosion inhibitor concentrations after 2-day pre-corrosion. The polarization curve of no pre-corrosion and 400 ppm$_w$ inhibitor is also displayed for comparison purpose.

This process is called cathodic area normalization in this study.

To realize the normalization, the ratio of cathodic reaction area (R) with and without a Fe_3C skeleton is required. This ratio can be obtained by studying the change in limiting current, which is assumed to depend only on the change in cathodic surface area (unaffected with CI as proved experimentally). This assumption was based on the condition that the mass transfer coefficient of hydrogen ion was unaffected in the cementite skeleton. Compared with 20 – 30 μm gap space in cementite skeleton (Fig. 8), the thickness of hydrogen mass transfer boundary layer was calculated being only *ca.* 3 μm in the studied flow condition [38], indicating the mass transfer coefficient of hydrogen ion remained the same in the cementite skeleton. Consequently, the cathodic area ratio can be deemed equal to the ratio of the limiting current, as shown by the following equation.

$$\frac{A_{with\ Fe_3C}}{A_{without\ Fe_3C}} = \frac{i_{\mathrm{lim},\ with\ Fe_3C}}{i_{\mathrm{lim},\ without\ Fe_3C}} = R \tag{5}$$

where "$A_{with\ Fe_3C}$" and "$A_{without\ Fe_3C}$" refer to the cathodic reaction area in the presence and absence of Fe_3C skeleton. "$i_{\mathrm{lim},\ with\ Fe_3C}$" and "$i_{\mathrm{lim},\ without\ Fe_3C}$" refer to cathodic limiting current in the presence and absence of Fe_3C skeleton. "R" refers to the ratio of cathodic reaction area with and without Fe_3C skeleton.

To determine the limiting currents and prepare for the subsequent cathodic area normalization, both the charge transfer part and limiting current part of the cathodic reaction were fitted to the measured polarization curves. A Tafel slope of 0.12 V/dec was adopted to fit the charge transfer part because the value has been widely reported for the

hydrogen ion reduction reaction on mild steel in CO_2 environments [39, 40]. The fitting curves for the inhibited cathodic polarization curves with and without pre-corrosion were displayed by dotted curves in Fig. 13 (a). The charge transfer part was perfectly fitted with the measured values, validating the selected value of the Tafel slope. With an excellent overall fitting with the measured curves, the limiting currents with and without the Fe_3C skeleton were obtained. According to Eq. (5), the ratio of cathodic area with and without the Fe_3C skeleton was determined as 4.0. Knowing this ratio, the cathodic curve with pre-corrosion can be normalized based on the cathodic area on the bare surface *via* dividing cathodic current by the ratio. The normalized cathodic curve was displayed by the dotted purple curve in Fig. 13 (b), with it almost overlapping with the cathodic curve without pre-corrosion; indicating that the cathodic reaction was already retarded to the same extent as that on the bare surface. The difference in the cathodic retardation before normalization was caused only by the cathodic area increase due to the exposed Fe_3C skeleton after pre-corrosion.

To verify the accuracy of the ratio of cathodic area obtained from the limiting currents, it was also estimated from the cross-sectional SEM images. It is assumed that the cathodic area equals the specimen surface area on the bare steel surface. After 2-day pre-corrosion, the cathodic reaction happened not only at the substrate, but also on the exposed Fe_3C. The Fe_3C skeleton can be analogized and simplified to columns whose area can be estimated, as illustrated in Fig. 14. The ratio of cathodic area can be simplified to the ratio of the perimeter of the red line to the length L as shown in Fig. 14, which can be calculated by the following equation:

$$R = \frac{A_{with\ Fe3C}}{A_{without\ Fe3C}} = \frac{Perimeter\ of\ the\ red\ line}{L} = \frac{2 * N * H + L}{L} \quad (6)$$

where N is the number of Fe_3C strips, H is the thickness of the Fe_3C skeleton, and L is the cross-sectional length at the selected site. Multiple specimens that experienced 2-day pre-corrosion were selected to estimate the cathodic area ratio using the above equation, a cross-section example of which is shown in Fig. 14. The thickness of the Fe_3C skeleton after 2-day pre-corrosion is *ca.* 40 μm, *i.e.*, $H \approx 40$ μm. The cross-sectional length at the selected site is 500 μm, *i.e.*, $L \approx 500$ μm. The number of Fe_3C strips was counted from the cross-sectional SEM image as shown in Fig. 14. By this method, the ratio of cathodic area with and without Fe_3C skeleton was determined as 3.9 ± 0.5 from multiple specimens. This value is consistent with the aforementioned ratio estimated *via* limiting currents, which validated that method for ratio determination. It also confirmed the feasibility of evaluating cathodic inhibition by normalizing the cathodic area when residual Fe_3C exists.

3.3.2. *Polarization curves analysis of X65 steel*

The potentiodynamic polarization curves of X65 steel under three different conditions, *i.e.* no pre-corrosion and no inhibitor, no pre-corrosion and 400 ppm_w inhibitor, and 2-day pre-corrosion and no inhibitor, are shown in Fig. 15. After adding corrosion inhibitor with bare steel, both anodic and cathodic reactions were retarded significantly, while the limiting current was unaffected compared to the condition without either pre-corrosion or corrosion inhibitor. As aforementioned, the corrosion rate was maximally inhibited by 400 ppm_w inhibitor, which indicates both anodic and cathodic reactions were retarded maximally. After 2-day pre-corrosion, the acceleration of limiting current was significantly limited compared with that of C1018 as there was minimal Fe_3C residue on the X65 specimen surface. Again, the anodic reaction showed very slight retardation due to local environment change.

The potentiodynamic polarization curves of X65 steel with different concentrations of corrosion inhibitor after 2-day pre-corrosion are displayed in Fig. 16. After 2-day pre-corrosion and 1-day inhibition with 100 ppm_w inhibitor, both anodic and cathodic reactions were retarded compared with 2-day pre-corrosion condition without inhibitor. They were retarded further when the inhibitor concentration was increased to 200 ppm_w. However, there was no significant further retardation from 200 ppm_w to 400 ppm_w, suggesting maximum inhibition was achieved on the specimen that experienced 2-day pre-corrosion. In comparison with the case of no pre-corrosion but 400 ppm_w inhibitor, the anodic reaction was retarded to the same extent as reflected by the overlapped anodic curves, similar to the case of C1018 steel. What was different compared to the C1018 steel was the retardation of the cathodic reaction. The cathodic reaction with pre-corrosion was almost inhibited to the same extent as that on the bare surface without cathodic area normalization. It is suggested that the detrimental effect of residual Fe_3C on cathodic inhibition was insignificant on X65 steel compared with that of C1018 steel due to almost no Fe_3C remaining on the surface after pre-corrosion.

It should be noted here that multiple polarization curves were conducted on WE #1 during the inhibition stage, which is not recommended in the presence of corrosion inhibitor considering the interference to the inhibited surface condition by polarization. In this work, the potential range of anodic polarization was within desorption potential (no desorption behaviour observed from polarization curves) [41], suggesting the desorption process was insignificant during polarization. A new dose of inhibitor was added immediately after the conduction of

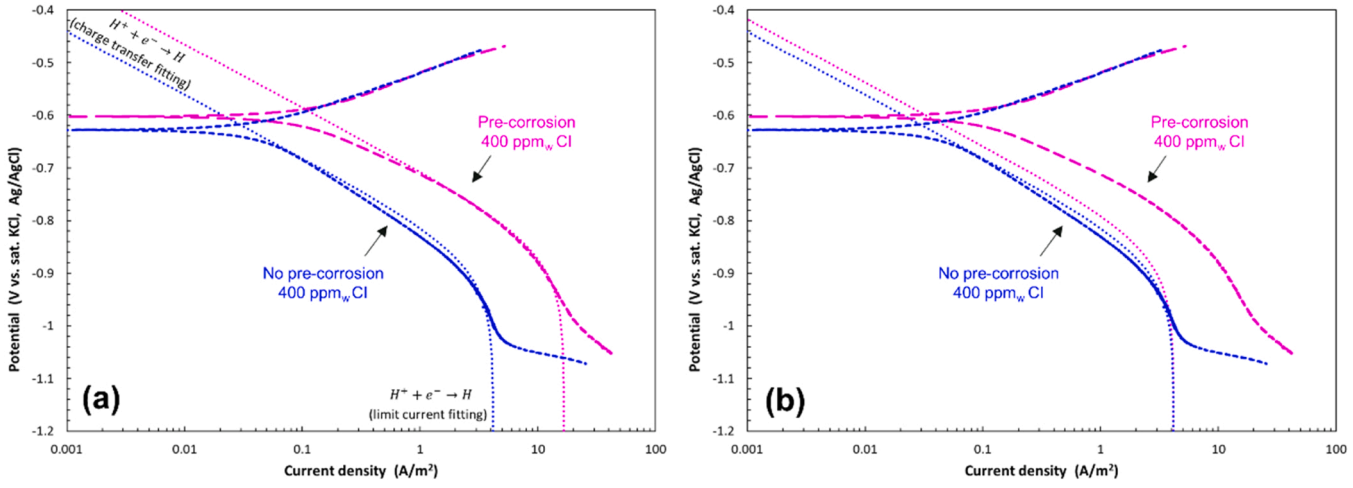

Fig. 13. The potentiodynamic polarization curves of C1018 steel with and without 2-day pre-corrosion in the presence of 400 ppm_w corrosion inhibitor: (a) before normalization; (b) after normalization (measured curves: dashed; fitting curves: dotted).

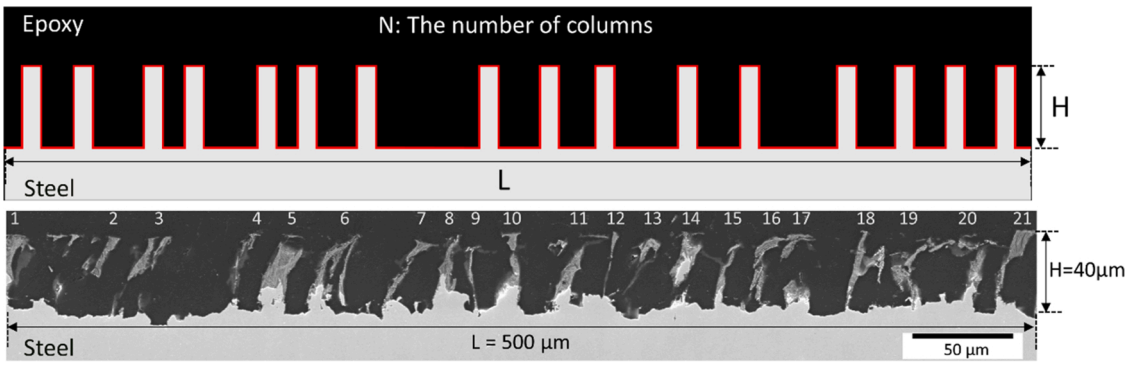

Fig. 14. Schematic for the estimation of cathodic reaction area ratio with and without cementite skeleton using cross-sectional SEM image.

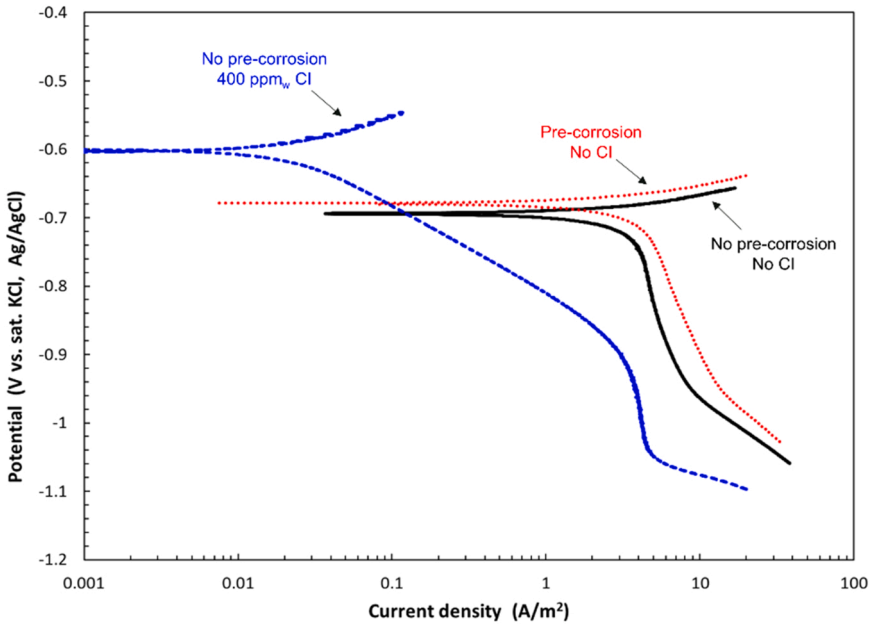

Fig. 15. The potentiodynamic polarization curves of X65 steel under three different conditions.

polarization sweeps and the corrosion rate and potential rapidly recovered back to the same level as that of WE #2, on which polarization sweep was not conducted until the end of the experiment. In addition, the polarization curves from WE #1 and WE #2 obtained at the end of the experiment showed excellent repeatability, which is provided as supplementary data. All these results indicated that the surface condition can rapidly recover to the original condition before polarization and subsequent measurements were not interfered by conducting polarization. The quick recovery could be associated with the quick adsorption kinetics of the commercial corrosion inhibitors used in this work and may not be valid with other such formulations.

3.4. *Effect of residual cementite on corrosion inhibition*

Due to the different steel microstructures and carbon contents between C1018 and X65 steels, significantly different conditions of residual cementite were observed after 2-day pre-corrosion in the studied conditions with well-controlled water chemistry. A *ca.* 40 μm Fe_3C skeleton was exposed and completely remained on the C1018 steel surface after 2-day pre-corrosion owing to the ferritic-pearlitic microstructure and high carbon content of C1018 steel. However, most of the Fe_3C particles fall off from the X65 steel surface during pre-corrosion and no measurable Fe_3C was detected by XRD, which was related to the low carbon content and the microstructure of small and dispersed cementite particles therein. In the presence of residual Fe_3C, the inhibition efficiency of C1018 with 100 ppm_w commercial inhibitor was significantly decreased, which was related to the galvanic coupling effect between ferrite and residual cementite serving as an additional cathodic area. This detrimental effect could be relieved if a higher inhibitor concentration was applied. However, the minimum inhibited corrosion rate (0.18 mm/year) in the presence of residual Fe_3C was always larger than that (0.08 mm/year) for the bare steel condition. In comparison, this detrimental effect was very limited in the case of X65 steel because of the insignificant amount of Fe_3C residue on the surface after pre-corrosion.

In terms of the inhibition mechanism in the presence of residual Fe_3C, it is clear that both anodic and cathodic reactions can be inhibited to the same extent as on bare steel, *i.e.*, maximum inhibition, with a sufficient concentration of corrosion inhibitor, such as 400 ppm_w in this study. Compared with bare steel condition, the lesser retardation of the cathodic reaction reflected in the polarization curve was only due to the additional cathodic area provided by the Fe_3C skeleton. This explained why the minimum inhibited corrosion rate with residual Fe_3C was always larger than that on bare steel. In summary, in the presence of residual Fe_3C, even though both anodic and cathodic reactions can be retarded maximally with a sufficient addition of corrosion inhibitor, the detrimental effect of residual Fe_3C cannot be completely eliminated due to its galvanic coupling effect.

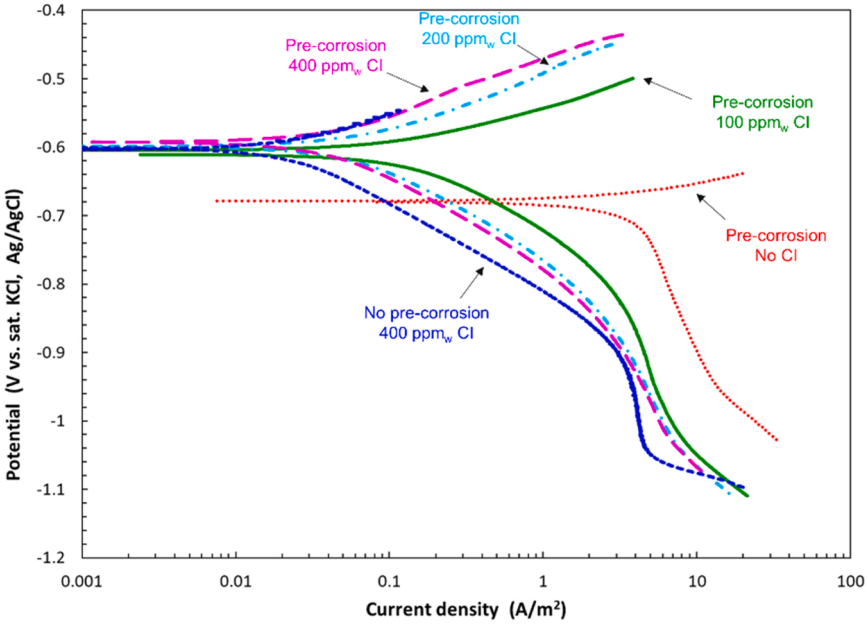

Fig. 16. The potentiodynamic polarization curves of X65 steel with different corrosion inhibitor concentrations after 2-day pre-corrosion. The polarization curve of no pre-corrosion and 400 ppm$_w$ inhibitor is also displayed for comparison purpose.

It is noteworthy that retardation of the cathodic reaction was easier than that of the anodic reaction according to the evolution of polarization curves of C1018 steel collected with different concentrations of corrosion inhibitor in Fig. 12. For instance, after injecting the first 100 ppm$_w$ dose, the cathodic reaction was close to being maximally inhibited, while the anodic reaction was much less retarded. It implies that the adsorption of inhibitor molecules on the outer Fe_3C skeleton (main cathodic reaction site) was easier than the adsorption at the inner substrate (anodic reaction site). The adsorption of inhibitor on the Fe_3C skeleton happened faster than the adsorption occurring on the substrate considering that the corrosion inhibitor had to diffuse through the Fe_3C skeleton in order to reach the substrate. This mass transfer process could be retarded by the Fe_3C skeleton acting as a diffusion barrier. Besides, the accelerated iron dissolution undergoing at the substrate made the adsorption of inhibitor more difficult than on the Fe_3C surface. Long-term experiments are required to test these hypotheses. In addition, the decrease in bulk concentration of corrosion inhibitor was observed in both experiments, which could be related to the inhibitor consumption *via* adsorbing on all interfaces in the glass cell without inhibitor replenishment. Therefore, experiments with continuous corrosion inhibitor injection will be of great value in maintaining a constant concentration in the bulk and simulating the inhibitor injection in real pipelines in the field. The issue of inhibitor consumption and the aforementioned hypotheses are being addressed in ongoing research.

4. Conclusions

The effect of residual cementite exposed after pre-corrosion on corrosion inhibition of an imidazoline-based commercial inhibitor package was quantitatively studied using C1018 and X65 steels with different microstructures and carbon contents in 5 wt% NaCl electrolyte with well-controlled water chemistry. The following conclusions can be drawn from this work:

(1) A *ca.* 40 μm residual Fe3C skeleton completely remained on the C1018 specimen surface after 2-day pre-corrosion, which was favored by its ferritic-pearlitic microstructure and higher carbon content. It significantly diminished the inhibition efficiency by acting as an additional cathodic area and consequently accelerating the iron dissolution rate through galvanic coupling. In comparison, this detrimental effect was insignificant for X65 steel because the amount of residual Fe3C after pre-corrosion was limited, with most detaching from the surface due to the small and dispersed particle microstructure and low carbon content.

(2) In the presence of residual Fe3C, both anodic and cathodic reactions can be inhibited to the same extent as on bare steel with a sufficient concentration of corrosion inhibitor. Compared with bare steel condition, the lesser retardation of the cathodic reaction reflected in the polarization curve was only due to the additional cathodic area provided by the Fe3C residue. The minimum inhibited corrosion rate with residual Fe3C was always larger than that on the bare steel due to the galvanic coupling effect.

CRediT authorship contribution statement

Shuai Ren: Methodology, Investigation, Writing – original draft. **Xi Wang:** Methodology, Writing – review & editing. **David Young:** Methodology, Writing – review & editing. **Maalek Mohamed-Said:** Resources, Funding acquisition, Writing – review & editing. **Bernardo Santos:** Investigation, Writing – review & editing. **Yi He:** Writing – review & editing. **Marc Singer:** Conceptualization, Supervision, Funding acquisition, Writing – review & editing.

Declaration of Competing Interest

The authors declare that they have no known competing financial interests or personal relationships that could have appeared to influence the work reported in this paper.

Data availability

Data will be made available on request.

Acknowledgments

This project has been supported by TotalEnergies transversal R&D project (MANA Project). The authors would like to thank Alexis Barxias

and Cody Shafer for their technical support at Institute for Corrosion and Multiphase Technology (ICMT) at Ohio University.

Appendix A. Supporting information

Supplementary data associated with this article can be found in the online version at doi:10.1016/j.corsci.2023.111382.

References

[1] R. Walker, Principles and prevention of corrosion, Mater. Des. 14 (1993) 207, https://doi.org/10.1016/0261-3069(93)90066-5.

[2] G. Koch, J. Varney, N. Thompson, O. Moghissi, M. Gould, J. Payer International measures of prevention, application, and economics of corrosion technologies study, 2016. ⟨http://impact.nace.org/⟩.

[3] E. McCafferty, Corrosion Inhibitors, in: Introd. to Corros. Sci., Springer New York, New York, NY, 2010, pp. 357–402, https://doi.org/10.1007/978-1-4419-0455-3.

[4] V.S. Sastri, Green Corrosion Inhibitors, John Wiley & Sons, Inc, Hoboken, NJ, USA, 2011, https://doi.org/10.1002/9781118015438.

[5] F. Farelas, B. Brown, S. Nesic, Iron carbide and its influence on the formation of protective iron carbonate in CO_2 corrosion of mild steel, paper no. 02291, in: CORROSION, NACE, 2013), Houston,TX, 2013.

[6] Z. Ma, Y. Yang, B. Brown, S. Nesic, M. Singer, Investigation of precipitation kinetics of $FeCO_3$ by EQCM, Corros. Sci. 141 (2018) 195–202, https://doi.org/10.1016/j.corsci.2018.06.017.

[7] W. Zhang, D. Young, B. Brown, C. Shafer, F. Lu, E. Anyanwu, M. Singer, An in-situ Raman study on the oxidation of mackinawite as a corrosion product layer formed on mild steel in marginally sour environments, Corros. Sci. 188 (2021), 109516, https://doi.org/10.1016/j.corsci.2021.109516.

[8] E. Gulbrandsen, S. Nesic, A. Stangeland, T. Burchardt, B. Sundfaer, S.M. Hesjevik, S. Skjerve, Effect of precorrosion on the performance of inhibitors for CO_2 corrosion of carbon steel, paper no. 98013, in: CORROSION, NACE, 1998), Houston,TX, 1998.

[9] B.S. Hou, Q.H. Zhang, Y.Y. Li, G.Y. Zhu, G.A. Zhang, Influence of corrosion products on the inhibition effect of pyrimidine derivative for the corrosion of carbon steel under supercritical CO_2 conditions, Corros. Sci. (2020), https://doi.org/10.1016/j.corsci.2020.108442.

[10] H. Sun, H. Fang, J. Davis, R. Hudgins, Investigation of Effects of Iron Sulfide on Corrosion and Inhibition of Carbon Steel in H_2S Containing Conditions, paper no. 1651, in: CORROSION 2012, NACE, Houston,TX, 2012.

[11] S. Ren, X. Wang, D. Young, S. Marc, M. Maalek, Mohamed-Said Gregory, M. Stroe, Effect of Cementite on the Corrosion Inhibition of Carbon Steel with Tetradecyl Phosphate Ester in CO_2 environment, paper no. 19309, in: AMPP Annual Conference+Expo 2023, AMPP, Houston, TX, 2023.

[12] M.-C. Lee, G. Simkovich, Electrical conduction behavior of cementite, Metall. Trans. A 18 (1987) 485–486, https://doi.org/10.1007/BF02648811.

[13] J. Owen, F. Ropital, G.R. Joshi, J. Kittel, R. Barker, Galvanic effects induced by siderite and cementite surface layers on carbon steel in aqueous CO_2 environments, Corros. Sci. 209 (2022), 110762, https://doi.org/10.1016/j.corsci.2022.110762.

[14] Y. Xiong, D. Fischer, F. Cao, J. Pacheco, Impact of pre-corrosion on corrosion inhibitor performance: Can we protect aged pipelines?, paper no. 8919, in: CORROSION NACE, 2017), Houston, TX, 2017.

[15] A.A. Al-Asadi, Iron Carbide Development and Its Effect on Inhibitor Performance, Ohio University, Master Thesis, 2014.

[16] H.H. Zhang, X. Pang, M. Zhou, C. Liu, L. Wei, K. Gao, The behavior of pre-corrosion effect on the performance of imidazoline-based inhibitor in 3 wt% NaCl solution saturated with CO_2, Appl. Surf. Sci. 356 (2015) 63–72, https://doi.org/10.1016/j.apsusc.2015.08.003.

[17] L.D. Paolinelli, T. Pérez, S.N. Simison, The effect of pre-corrosion and steel microstructure on inhibitor performance in CO_2 corrosion, Corros. Sci. 50 (2008) 2456–2464, https://doi.org/10.1016/j.corsci.2008.06.031.

[18] L.D. Paolinelli, T. Pérez, S.N. Simison, The incidence of chromium-rich corrosion products on the efficiency of an imidazoline-based inhibitor used for CO_2 corrosion prevention, Mater. Chem. Phys. 126 (2011) 938–947, https://doi.org/10.1016/j.matchemphys.2010.12.001.

[19] D.A. López, S.N. Simison, S.R. de Sánchez, Inhibitors performance in CO_2 corrosion, Corros. Sci. 47 (2005) 735–755, https://doi.org/10.1016/j.corsci.2004.07.010.

[20] A. Shamsa, R. Barker, Y. Hua, E. Barmatov, T.L. Hughes, A. Neville, Impact of corrosion products on performance of imidazoline corrosion inhibitor on X65 carbon steel in CO_2 environments, Corros. Sci. 185 (2021), 109423, https://doi.org/10.1016/j.corsci.2021.109423.

[21] E. Barmatov, T.L. Hughes, Effect of corrosion products and turbulent flow on inhibition efficiency of propargyl alcohol on AISI 1018 mild carbon steel in 4 M hydrochloric acid, Corros. Sci. 123 (2017) 170–181, https://doi.org/10.1016/j.corsci.2017.04.020.

[22] R. Nyborg, E. Gulbrandsen, T. Loeland, K. Nisancioglu, Effect of steel microstructure and composition on inhibition of CO_2 corrosion, paper no. 23, in: CORROSION, NACE, 2000), Houston, TX, 2000.

[23] H. Mansoori, D. Young, B. Brown, S. Nesic, M. Singer, Effect of $CaCO_3$-saturated solution on CO_2 corrosion of mild steel explored in a system with controlled water chemistry and well-defined mass transfer conditions, Corros. Sci. 158 (2019), 108078, https://doi.org/10.1016/j.corsci.2019.07.004.

[24] H. Mansoori, B. Brown, D. Young, S. Nešić, M. Singer, Effect of $FexCa_yCO_3$ and $CaCO_3$ Scales on the CO_2 Corrosion of Mild Steel, Corrosion 75 (2019) 1434–1449, https://doi.org/10.5006/3290.

[25] H. Sarac, M.A. Patrick, A.A. Wragg, Physical properties of the ternary electrolyte potassium ferri-ferrocyanide in aqueous sodium hydroxide solution in the range 10–90 °C, J. Appl. Electrochem. 23 (1993) 51–55, https://doi.org/10.1007/BF00241575.

[26] R.P.W.M. Jacobs, R.O.H. Grant, J. Kwant, J.M. Marquenie, E. Mentzer, The Composition of Produced Water from Shell Operated Oil and Gas Production in the North Sea, in: Prod. Water, Springer, US, Boston, MA, 1992, pp. 13–21, https://doi.org/10.1007/978-1-4615-2902-6_2.

[27] H. Mansoori, D. Young, B. Brown, S. Nesic, M. Singer, Effect of $CaCO_3$-saturated solution on CO_2 corrosion of mild steel explored in a system with controlled water chemistry and well-defined mass transfer conditions, Corros. Sci. 158 (2019), 108078, https://doi.org/10.1016/j.corsci.2019.07.004.

[28] M. Stern, A.L. Geary, Electrochemical polarization, J. Electrochem. Soc. 104 (1957) 56, https://doi.org/10.1149/1.2428496.

[29] L.K. Wang, Colorimetric method for the analysis of residual anionic or cationic surfactants, US Pat. 3,992 149 (1976).

[30] Y.M. Evtushenko, V.M. Ivanov, B.E. Zaitsev, Photometric determination of octadecylamine with methyl orange, J. Anal. Chem. 57 (2002) 8–11, https://doi.org/10.1023/A:1013693120902.

[31] T. Jackson, V. Jonathan, Selective Loss of Bulk Corrosion Inhibitor Species when Exposed to Glass, Plastic, and Steel, in: CORROSION 2020, paper no. 14999, NACE, Houston, TX, 2020.

[32] A. Kahyarian, S. Nesic, A new narrative for CO_2 corrosion of mild steel, J. Electrochem. Soc. 166 (2019) C3048–C3063, https://doi.org/10.1149/2.0071911jes.

[33] A. Kahyarian, S. Nesic, On the mechanism of carbon dioxide corrosion of mild steel: experimental investigation and mathematical modeling at elevated pressures and non-ideal solutions, Corros. Sci. 173 (2020), 108719, https://doi.org/10.1016/j.corsci.2020.108719.

[34] S. Ren, Y. He, Z. Belarbi, X. Wang, D. Young, M. Singer, M. Mohamed-Said, S. Camperos, Methodology of Corrosion Inhibitor Characterization Applied to Phosphate Ester and Tetrahydropyrimidinium Model Compounds, paper no. 16443, in: AMPP Annual Conference+Expo 2021, AMPP, Houston, TX, 2021.

[35] X. Wang, S. Ren, Y. He, D. Young, M. Singer, M. Mohamed-Said, S. Camperos, Effect of Organic Solvent on Corrosion Inhibition of Mild Steel in CO_2 Environment, paper no. 17942, in: AMPP Annual Conference+Expo, AMPP 2022, Houston, TX, 2022.

[36] J.M. Dominguez Olivo, D. Young, B. Brown, S. Nesic, An Improved Methodology to Assess the Performance of Organic Corrosion Inhibitors, paper no. 14984, in: CORROSION, NACE, 2020, Houston, TX, 2020.

[37] J.M. Olivo Domínguez, S. Cao, S. Nesic, D. Young, B. Brown, Effect of Corrosion Inhibitor Head Group on the Electrochemical Processes Governing CO_2 Corrosion. CORROSION 2020, paper no. 14925, NACE, Houston, TX, 2020.

[38] S. Nesic, F. Madani Sani, Calculation of cathodic limiting current density in weak acids: part I. Aqueous CO_2 solutions, J. Electrochem. Soc. 170 (2023), 011504, https://doi.org/10.1149/1945-7111/acb4e5.

[39] N. Pentland, J.O. Bockris, E. Sheldon, Hydrogen evolution reaction on copper, gold, molybdenum, palladium, rhodium, and iron, J. Electrochem. Soc. 104 (1957) 182, https://doi.org/10.1149/1.2428530.

[40] A. Kahyarian, B. Brown, S. Nesic, Mechanism of the hydrogen evolution reaction in mildly acidic environments on gold, J. Electrochem. Soc. 164 (2017) H365–H374, https://doi.org/10.1149/2.1061706jes.

[41] V.J. Drazic, D.M. Drazic, Influence of the metal dissolution rate on the anion and inhibitor adsorption, 7 Th Eur. Symp. Corros. Inhib. (1990) 99–110.